Heat and Mass Transfer
https://doi.org/10.1007/s00231-022-03303-1

ORIGINAL ARTICLE

Experimental study on migration and heat transfer characteristics of three potential molten salts leaking into tank foundation materials

Yuhang Zuo[1] · Hao Zhou[1] · Mingrui Zhang[1] · Fangzheng Cheng[1] · Hua Shi[1]

Received: 20 June 2022 / Accepted: 28 September 2022

Abstract

The leakage of molten salt tanks has attracted great attention in molten salt tower concentrating solar power plants. The current research on the leakage characteristics of molten salt mainly focuses on Solar Salt, and there is no report on the leakage characteristics of molten salt with great application potential, which is crucial to the design of molten salt tanks and their foundations in the future. In addition, there is no unified explanation for the morphological characteristics of the agglomerates formed after the molten salt leakage. In this paper, the migration and heat transfer characteristics of three potential molten salts (60–10-20–20 wt% KNO_3-$NaNO_3$-$LiNO_3$-$Ca(NO_3)_2.4H_2O$, 7.5–23.9–68.6 wt% NaCl–KCl-$ZnCl_2$, 32.1–33.4–34.5 wt% Li_2CO_3–Na_2CO_3–K_2CO_3) leaking into the thermal tank foundation material are experimentally studied and compared with Solar Salt. The results indicate that both the operating temperature and molten salt type significantly affect the temperature rising rate of tank foundation and migration characteristics of molten salt. Increasing the operating temperature, the average temperature rising rate, maximum migration depth, maximum migration width and migration speed respectively increase, increase, decrease and increase. Compared with Solar Salt, the maximum migration depths of the three potential molten salts increase 56.3%, -11.6%, and -50.2%, and the maximum migration widths increase -22.7%, -16.7% and -2.7%, respectively. In addition, a model explaining the solidification and agglomeration of the molten salt is proposed and well verified by the experimental results.

Nomenclature

Greek symbols

α	Volume fraction
λ	Thermal conductivity (W/(m.K))
δ	Thickness (m)

Roman symbols

L_1	Distance between the top of the solid molten salt block and the top of the fillers (mm)
L_2	Length of the solid molten salt block (mm)
L_3	Maximum migration depth (mm)
q	Heat flux (W/m^2)
T_{op}	Operating temperature (℃)
T	Temperature (℃)
ΔT	Temperature difference in steady state after and before the molten salt leakage (℃)
TRR	Temperature rising rate (℃/s)
t	Time (min)
U	Voltage (V)
W_m	Maximum migration width (mm)
z	Coordinate (mm)

Abbreviations

CSP	Concentrating solar power
TES	Thermal energy storage
CSF	Continuous surface force
LECA	Light expanded clay aggregate
SMSB	Solid molten salt block

1 Introduction

Among many renewable energy utilization technologies, concentrating solar power (CSP) shows an encouraging prospect for its high efficiency, low operating cost and good scale-up potential [1], which has been one of the fastest growing commercial technologies in the past few decades. By 2050, CSP will account for 11.3% of global power

✉ Hao Zhou
zhouhao@zju.edu.cn

[1] State Key Laboratory of Clean Energy Utilization, Institute for Thermal Power Engineering, Zhejiang University, Hangzhou 310027, China

Published online: 02 November 2022

generation [2, 3]. The inherent advantage of CSP technology over other renewable energy technologies (such as photovoltaic and wind energy) lies in its integration with thermal energy storage (TES) system solving the intermittent and schedulability of the technology, leading to a significant improvement of its reliability and economic competitiveness [1, 4]. At present, 45.5% of the CSP plants during operation in the world are equipped with TES systems [5].

The molten salt is recognized as one of the best heat transfer/storage fluid choices in CSP plants [6]. There are currently three nitrate/nitrite molten salts that are widely used commercially in tower CSP plants, including Solar Salt, Hitec and Hitec XL [1, 7, 8]. Considering the thermal stability of nitrate/nitrite molten salts at high temperatures, the most efficient and cost-competitive tower CSP plant can only transfer heat to the conventional steam Rankine power cycle at 565 °C, the thermal-electric conversion efficiency of which is only 35–42% [9]. The recent roadmap [10] chooses the sCO_2 Brayton cycle as the preferred way to increase the thermal-electric conversion efficiency of the tower CSP plant. The cycle works at a temperature above 700 °C, and its efficiency exceeds 50%. Thus, it is crucial to develop molten salts with more suitable properties. That is, higher heat capacity, higher density, better thermal stability and lower corrosiveness to the container materials [11]. The chloride blends and carbonate blends seem to be the most viable options for high-temperature molten salts [12]. Among them, 7.5–23.9–68.6 wt% NaCl–KCl-$ZnCl_2$ and 32.1–33.4–34.5 wt% Li_2CO_3–Na_2CO_3–K_2CO_3 have attracted many researchers' interests. According to the research results, they can be used above 650 ℃ and 800 ℃ respectively [13–16]. At present, to prevent Solar Salt with a melting point above 200 °C from solidifying, the heat tracing system, higher standards of the insulation system and emergency response system are needed in the tower CSP plant, increasing the construction and operation costs of the plant. Thus, the development of molten salt with a low melting point also requires effort. The quaternary nitrate blends 60–10-20–20 wt% KNO_3-$NaNO_3$-$LiNO_3$-$Ca(NO_3)_2.4H_2O$ proposed by Ren et al. [17] has a melting point of about 90 °C and a decomposition temperature above 600 °C. Besides, its other thermophysical properties are also comparable to Solar Salt, which means that it is a promising heat transfer/storage fluid for CSP plants.

During the operation of molten salt tanks, the primary environmental pollution is the emission of nitrogen oxides arising from high-temperature decomposition and the penetration of molten salt to the tank foundation after its leakage [18]. After the molten salt leaks from the tank, it will migrate in the tank foundation material and even contaminate the soil and groundwater. Due to the relatively low temperature of the tank foundation, the molten salt will not only migrate around and below after leakage, but also solidify in the tank foundation. The process is a complex multiphase flow process in porous media, involving fluid dynamics, heat transfer, and phase change [19]. Researchers have done some research in the related fields. Dawson et al. [20] applied the volume of fluid (VOF) model and moving boundary model to numerically study the crystalline deposits from the dripping salt solution. Song et al. [21] theoretically and experimentally studied the lateral freezing of the aqueous ammonium chloride solution in a porous medium. Weisbrod et al. [22] used the light transmission system to experimentally study the migration of concentrated sodium nitrate solution in different silica sands, and obtained the influence of solution density and effective contact angle on the migration process. Shan et al. [23] used VOF and continuous surface force (CSF) model to simulate the leakage of Solar Salt to the soil surface. The results showed that the leakage temperature and speed affected both the radius and thickness of the solidification layer, while the radius of the leakage aperture mainly affected the former. Compared with the molten salt SYSU-N1 developed by themselves, the radius of the solidified layer of Solar Salt is larger. Wu et al. [24] simulated the process of molten salt leaking into cold soil by VOF. The results showed that the maximum migration radius increased with the increase of the inlet temperature or inlet velocity, while decreased with the increase of the porosity. The maximum migration depth increased with the increase of the inlet temperature or porosity, while not affected by the inlet velocity. Zhang et al. [25] experimentally and numerically studied the process of molten salt leaking into the cold sand. It was found that larger porosity and particle size or higher inlet temperature increased and decreased the maximum migration depth and diameter, respectively. Zhou et al. [19] experimentally studied the leakage process of molten salt in the thermal porous tank foundation material, and the influences of the porosity, operating temperature, leakage aperture and leaking mass on that were explored. The results showed that the most critical factor was the operating temperature.

From the above literature review, firstly, the currently available articles on the migration and heat transfer characteristics after the molten salt leakage are mainly carried out in cold porous media. However, the molten salt will leak into the hot tank foundation material in actual CSP plants when the molten salt tanks rupture. Secondly, the current research on the migration and heat transfer characteristics of molten salt mainly focuses on Solar Salt, and there is no report on the leakage characteristics of molten salt with great application potential, which is crucial to the design of molten salt tanks and their foundations in the future. Finally, there is no unified explanation for the morphological characteristics of the agglomerates formed after the molten salt leakage.. To fill the above gaps, the migration and heat transfer characteristics of three potential molten salts

(60–10-20–20 wt% KNO_3-$NaNO_3$-$LiNO_3$-$Ca(NO_3)_2.4H_2O$, 7.5–23.9–68.6 wt% NaCl–KCl-$ZnCl_2$, 32.1–33.4–34.5 wt% Li_2CO_3–Na_2CO_3–K_2CO_3) leaking into the thermal tank foundation material have been experimentally studied and compared with Solar Salt in this paper. In addition, a model explaining the solidification and agglomeration of the molten salt is proposed and verified. The research results are of great benefit to better understanding, preventing and treating the molten salt tank leakage accidents.

2 Experimental materials and methods

2.1 Materials

Four molten salts are used in this paper, namely Solar Salt (60–40 wt% $NaNO_3$-KNO_3), quaternary nitrate blends (60–10-20–20 wt% KNO_3-$NaNO_3$-$LiNO_3$-$Ca(NO_3)_2.4H_2O$), ternary chloride blends (7.5–23.9–68.6 wt% NaCl–KCl-$ZnCl_2$) and ternary carbonate blends (32.1–33.4–34.5 wt% Li_2CO_3–Na_2CO_3–K_2CO_3). The properties [2, 7–9, 12–14, 17, 26]of the four molten salts are shown in Table 1, and the experimental conditions are shown in Table 2. Among them, the Solar Salt provided by Zhejiang Lianda Chemical Co., Ltd. has a purity above 99.5%. The other three molten salts are prepared by weighing, mixing, melting and cooling steps according to their composition ratios. The purity of each composition exceeds 99.0%.

As shown in Fig. 1, the typical molten salt tank foundation in the CSP plant is usually composed of multiple layers of thermal insulation materials and concrete slabs with a ventilation system. On the one hand, the ventilation system prevents the concrete slab from being overheating to weaken its strength or produce cracks. On the other hand, the ventilation system also prevents the moisture in the tank foundation from evaporating and avoids weakening its bearing capacity, causing uneven settlement or even rupture of the tank [27]. Due to the low cost, light weight and good thermal insulation, light expanded clay aggregate (LECA) is widely used as one of the thermal insulation materials for molten salt tanks [28]. Therefore, the LECA with different particle sizes is prepared and used as the porous tank foundation material to restore the leakage process of the molten salt tank. The particle size distribution, density and porosity of the LECA are shown in Table 3.

2.2 Methods

In order to conduct the study of the leakage process of the molten salt in the tank foundation, a lab-scale experimental system as shown in Fig. 2 was designed and built. The experimental process can be divided into three stages: (1) filler heating, (2) high temperature molten salt preparation and its migration and phase change, (3) filler cooling and post-treatment. In the first stage, the mixed LECAs are filled into the tank and heated to a steady state. Heating of the fillers is achieved by the ceramic sheathed electrical resistance heater with a temperature range of 30 °C–800 °C. The on-site molten salt tank foundation is heated by the molten salt tank bottom plate, to restore the situation, the heater is installed in the tank cover plate in this work to heat the fillers from top to bottom. The inner effective space of the tank containing the fillers is 345 mm in diameter and 760 mm in height. To prevent excessive heat dissipation of the fillers, the side wall and cover plate of the tank are insulated with refractory bricks. Since the heater height is 60 mm, the actual final fill height is 700 mm. The temperature distribution and evolution of the filler during the experiment are measured by 16 K-type thermocouples with an accuracy of ± 1.0 °C. They are inserted into the center of the tank from the holes on the side wall, and the vertical interval between adjacent thermocouples is 40 mm. The temperature data obtained is recorded and saved by the Agilent 34,970 data logger. Its temperature measurement accuracy is ± 1.0 ℃, so the total accuracy of temperature measurement is ± 2.0 °C. The basis for reaching steady state during the heating stage

Table 1 Properties of the four molten salts

Property	Solar Salt	Quaternary nitrate blends	Ternary chloride blends	Ternary carbonate blends
Composition	60 wt% $NaNO_3$ 40 wt% KNO_3	60 wt% KNO_3 10 wt% $NaNO_3$ 20 wt% $LiNO_3$ 20 wt% $Ca(NO_3)_2.4H_2O$	7.5 wt% NaCl 23.9 wt% KCl 68.6 wt% $ZnCl_2$	32.1 wt% Li_2CO_3 33.4 wt% Na_2CO_3 34.5 wt% K_2CO_3
Density (kg/m^3) (at 300℃)	1899	1868	2347	2071 (at 450 ℃)
Melting point (℃)	220	85.4	210.3	405
Stability limit (℃)	565	> 600	850	673
Latent heat (kJ/kg)	113.03	106.9	73.89	223
Thermal conductivity (w/(m.K)) (at 300 ℃)	0.500	0.537	0.381	0.454 (at 450 ℃)
Heat capacity (J/(kg.K)) (at 300 ℃)	1495	1554	900	1700 (avg.400–827 ℃)
Viscosity (Pa.s) (at 300 ℃)	0.0033	0.0031	0.0131	0.0043 (at 800 ℃)

Table 2 Experimental conditions

Case	Molten salt	Operating temperature (℃)
A	60–40 wt% $NaNO_3$-KNO_3	500
B1	60–10-20–20 wt% KNO_3-$NaNO_3$-$LiNO_3$-$Ca(NO_3)_2.4H_2O$	300
B2	60–10-20–20 wt% KNO_3-$NaNO_3$-$LiNO_3$-$Ca(NO_3)_2.4H_2O$	400
B3	60–10-20–20 wt% KNO_3-$NaNO_3$-$LiNO_3$-$Ca(NO_3)_2.4H_2O$	500
B4	60–10-20–20 wt% KNO_3-$NaNO_3$-$LiNO_3$-$Ca(NO_3)_2.4H_2O$	550
C1	7.5–23.9–68.6 wt% NaCl–KCl-$ZnCl_2$	300
C2	7.5–23.9–68.6 wt% NaCl–KCl-$ZnCl_2$	400
C3	7.5–23.9–68.6 wt% NaCl–KCl-$ZnCl_2$	500
C4	7.5–23.9–68.6 wt% NaCl–KCl-$ZnCl_2$	550
D1	32.1–33.4–34.5 wt% Li_2CO_3–Na_2CO_3–K_2CO_3	450
D2	32.1–33.4–34.5 wt% Li_2CO_3–Na_2CO_3–K_2CO_3	500
D3	32.1–33.4–34.5 wt% Li_2CO_3–Na_2CO_3–K_2CO_3	550
D4	32.1–33.4–34.5 wt% Li_2CO_3–Na_2CO_3–K_2CO_3	600

is that the temperature change of the filler does not exceed 0.5 °C within 3 h. In the second stage, 600 g molten salt is first weighed with an electronic balance with an accuracy of ± 0.1 g and put into the crucible, then another crucible with a 10 mm round hole at the bottom is taken, and finally the two crucibles are put into the muffle furnace together. After setting the final temperature of the muffle furnace to be the same as the final temperature of the heater, the heating of the molten salt is started. During this period, the molten salt is gradually melted and held for 5 h after reaching the set temperature. After that, we pull up the tank cover plate, and take out the bottom opening crucible from the muffle furnace and place it in the center above the fillers, then take out the high temperature molten salt and pour it into the fillers through the bottom opening crucible. The cover plate is then quickly covered, after which the molten salt migrates and solidifies in the fillers. When the filler temperature reaches steady state again, the third stage starts. At this point, the heater in the cover plate is turned off and the fillers are allowed to cool naturally. The molten salt poured into the tank will adhere to a part of the fillers to form the solid molten salt block during the experiment. After cooling, the tank bottom plate is opened to release the unagglomerated fillers, and the formed solid molten salt block will hang on the thermocouple. Finally, the solid molten salt block is taken out and the relevant parameters are measured by a tape measure with an accuracy of ± 0.5 mm.

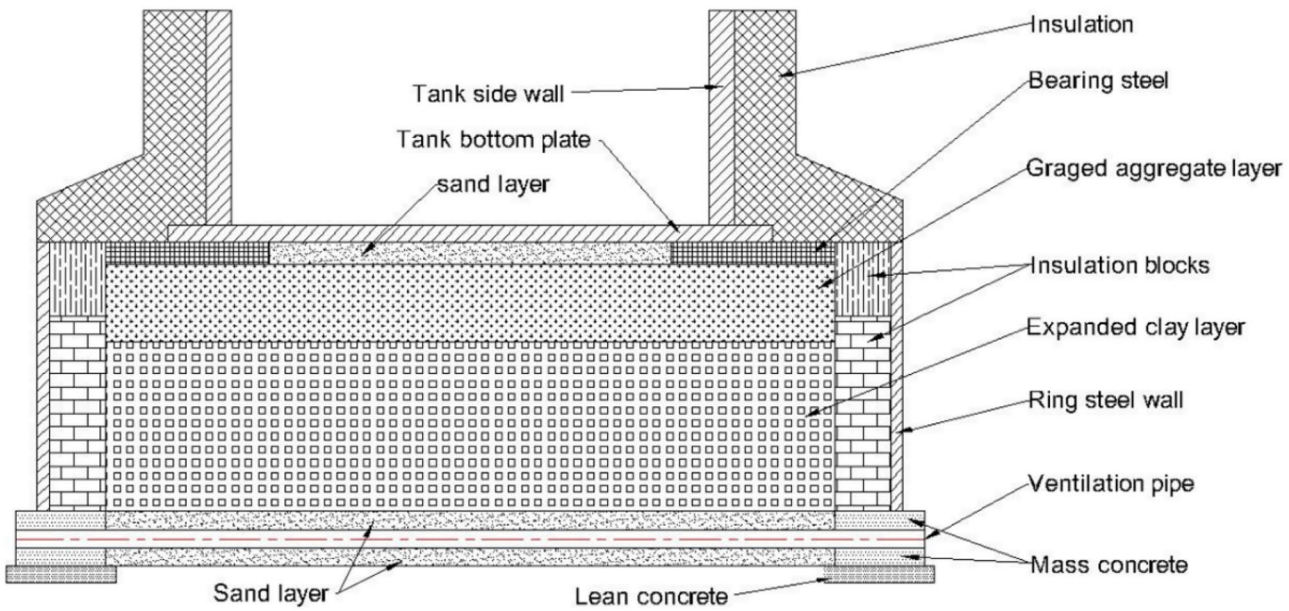

Fig. 1 Schematic diagram of the tank foundation structure of an actual molten salt tank

Table 3 Properties of the LECA

Properties	Value
Particle size distribution	3.35–6.3 mm 39% 6.3–8 mm 31% 8–10 mm 13% 10–20 mm 17%
Bulk density (kg/m^3)	596.73
Porosity (%)	35.8

3 Results and discussion

3.1 Heat transfer characteristics

3.1.1 Temperature distribution and evolution

Figure 3 presents the temperature distribution and evolution of the tank foundation during the whole experimental process of case A. In the heating process, due to the presence of the top heater, the tank foundation is heated successively from top to bottom until the temperature distribution reaches a steady state. The closer to the top, the higher the steady temperature and the less the time to reach the steady temperature. For example, at $z=40$ mm, $z=80$ mm and $z=120$ mm, the steady temperatures are respectively 469.5 °C, 309.7 °C and 225.2 °C, and the time to reach the steady temperature in these positions are respectively 372.3 min, 1026.0 min and 1183.3 min. The entire tank foundation reaches the steady state after about 30 h. During the migration and phase change process of the molten salt, the temperature of the molten salt is high initially and it migrates rapidly in the fillers, the temperature at each position of the molten salt flowing through first rises rapidly to the maximum value, and then decreases rapidly for the molten salt continues to flow down and dissipates heat. When the molten salt migrates down to a specific position, its temperature drops below the melting point and the molten salt starts to solidify, hindering the upper molten salt from migrating downward and causing the molten salt to accumulate. Finally, the temperature distribution of the entire tank foundation becomes steady again. In the cooling process, the tank foundation temperature drops rapidly to the ambient temperature. Because of the higher temperature and heat dissipation, the temperature drops faster near the top. As shown in Fig. 4, the steady tank foundation temperature after the leakage process is higher than that before the leakage process, and the area with large temperature difference is exactly the area where the molten salt agglomerates (115 mm $\le z \le$ 448 mm). The reason for this phenomenon is that the air in the pores of the LECAs in this area is occupied by the solidified molten salt with better thermal conductivity. The effective medium theory equation

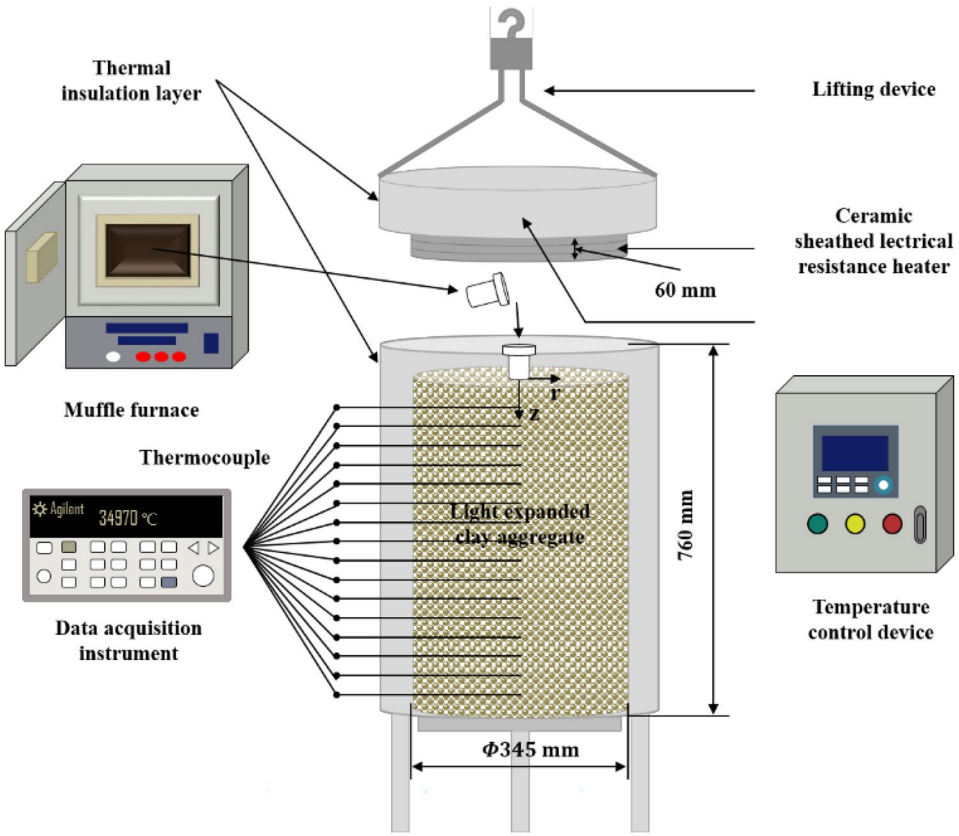

Fig. 2 Schematic diagram of the lab-scale molten salt leakage experimental system

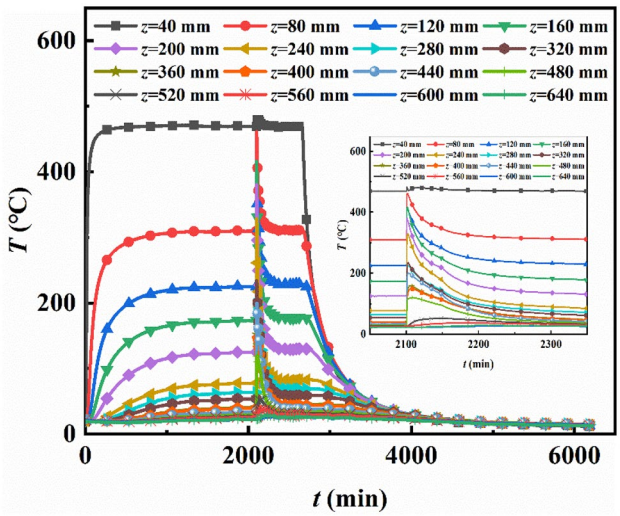

Fig. 3 Temperature distribution and evolution of the tank foundation during the whole experimental process. (Case A: Solar Salt, T_{op} = 500 ℃)

as Eq. (1) can be used to obtain the effective thermal conductivity of porous fillers [19].

$$\left(1-\alpha_2\right)\frac{\lambda_1-\lambda_e}{\lambda_1+2\lambda_2}+\alpha_2\frac{\lambda_2-\lambda_e}{\lambda_2+2\lambda_e}=0 \tag{1}$$

Equation (1) can be transformed into Eq. (2).

$$\lambda_e=\frac{1}{4}\left(\left(3\alpha_2-1\right)\lambda_2+\left(3\left(1-\alpha_2\right)-1\right)\lambda_1+\sqrt{\left(\left(3\alpha_2-1\right)\lambda_2+\left(3\left(1-\alpha_2\right)-1\right)\lambda_1\right)^2+8\lambda_1\lambda_2}\right) \tag{2}$$

where λ_e, λ_1 and λ_2 are respectively the effective thermal conductivity, thermal conductivity of the fillers and thermal conductivity of the air, W/(m.K). α_2 is the volume fraction of the air.

When the molten salt leaks into the tank foundation material, the air in the fillers pores is occupied by molten salt. The thermal conductivity of molten salt is better than that of air. According to Eq. (2), the effective thermal conductivity of the fillers increases. Considering that the side wall of the tank is made of thick thermal insulation material, the fillers can be regarded as a one-dimensional heat conduction system similar to a multilayer flat wall. According to Fourier's law, the heat flux of the multilayer flat wall can be expressed as Eq. (3).

$$q=\frac{T_1-T_n}{\sum_{i=1}^{n}\frac{\delta_i}{\lambda_i}} \tag{3}$$

For each layer flat wall, the heat flux can be obtained by Eq. (4).

$$q=\lambda_i\frac{T_{i-}T_{i+1}}{\delta_i} \tag{4}$$

where q is the heat flux, W/m2, T_1 and T_n represent the temperature of the top and bottom of the fillers, respectively, δ_i is the thickness of layer i, m, and λ_i is the thermal conductivity, W/(m.K).

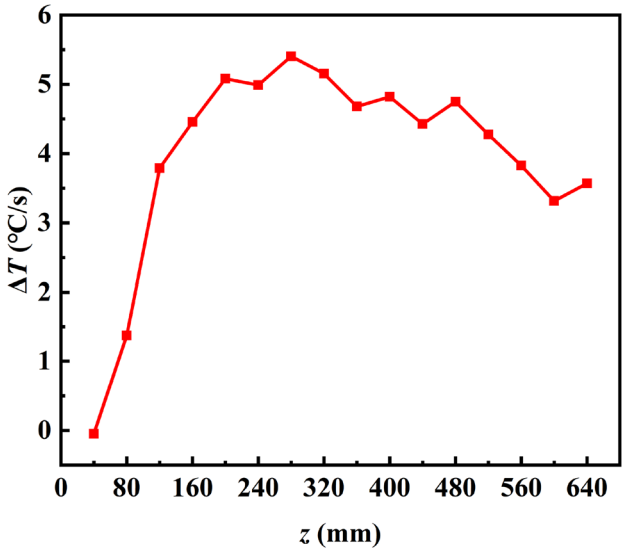

Fig. 4 Difference between the steady-state temperature of each measuring point after the molten salt leakage and the steady-state temperature before the leakage. (Case A: Solar Salt, T_{op} = 500 ℃)

Since the temperatures on the top and bottom of the filler is almost constant, according to Eq. (3), the heat flux increases after the molten salt leaks. According to Eq. (4), the temperature gradient of the fillers without molten salt increases, while the temperature gradient of the fillers with molten salt decreases. Therefore, the equilibrium temperature of the fillers increases after the molten salt leaks.

Figure 5 presents the steady temperature distribution of the tank foundation after the heating process at different operating temperatures. It can be seen that the temperature of the upper part of the tank foundation increases significantly as the operating temperature increases, while only a small change is found in the lower part. In addition, due to the higher temperature and heat dissipation, the temperature gradient of the upper part is significantly larger than that of the lower part. As shown in Table 4, the temperature gradient of the upper part (40 mm ≤ z ≤ 400 mm) is one order of magnitude larger than that of the lower part (400 mm ≤ z ≤ 640 mm).

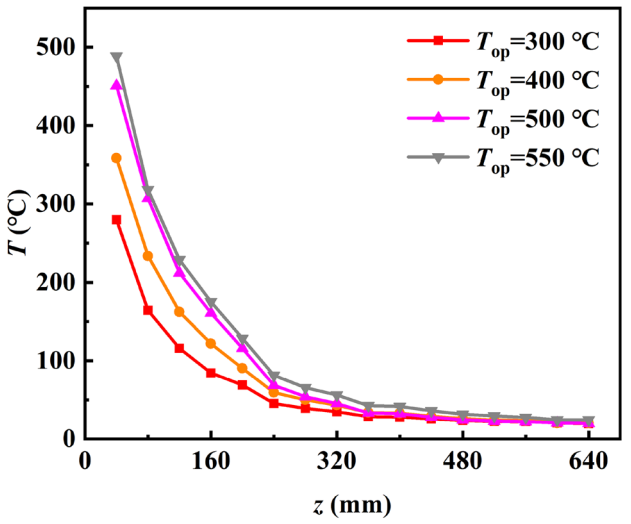

Fig. 5 Steady temperature distribution of the tank foundation after the heating process at different operating temperatures

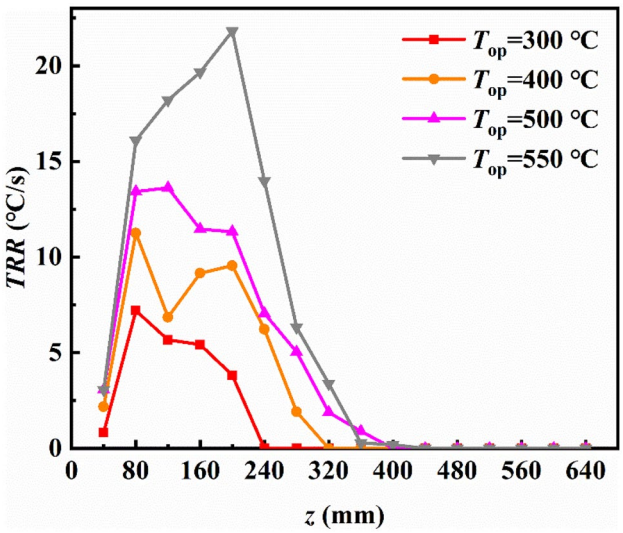

Fig. 6 Average temperature rising rate of each measuring point of the tank foundation at different operating temperatures. (7.5–23.9–68.6 wt% NaCl–KCl-$ZnCl_2$)

3.1.2 Temperature rising rate

The average temperature rising rate *TRR* of each thermocouple within 10 s after contacting the molten salt is shown in Fig. 6. When the operating temperature is 300 ℃, 400 ℃, 500 ℃ and 550 ℃, the maximum migration depth of 7.5–23.9–68.6 wt% NaCl–KCl-$ZnCl_2$ is 247 mm, 304 mm, 396 mm and 405 mm, respectively. Therefore, it can be seen that *TRR* of the position below the maximum migration depth is almost zero no matter what the operating temperature is. In the area of the molten salt flowing through, *TRR* from top to bottom increases first and then decreases. This is mainly because the temperature and heat dissipation at the top are high, so the temperature rising rates are low. At the bottom, the temperature of the molten salt is already low, and the amount of molten salt flowing in is small for the downward flow of the molten salt is hindered, so *TRR* is also low. In addition, it can be noticed that as the operating temperature increases, *TRR* in the area increases and the position of the highest *TRR* gradually shifts downward. The latter is mainly caused for the molten salt solidification position is closer to the bottom as the operating temperature increases.

Table 4 Steady temperature gradient of the tank foundation after heating process

Case	Temperature gradient (℃/mm)	
	40 mm ≤ *z* ≤ 400 mm	400 mm ≤ *z* ≤ 640 mm
C1	0.70	0.02
C2	0.90	0.03
C3	1.16	0.03
C4	1.24	0.05

Figure 7 presents the average temperature rising rate of all the thermocouples within 10 s after contacting the molten salt at different operating temperatures. *TRR* of the tank foundation under the three molten salts increases with the operating temperature increase. From 300 °C to 550 °C, *TRR* of 60–10-20–20 wt% KNO_3-$NaNO_3$-$LiNO_3$-$Ca(NO_3)_2.4H_2O$ and 7.5–23.9–68.6 wt% NaCl–KCl-$ZnCl_2$ increases from 5.43 °C/s, 1.44 °C/s to 11.78 °C/s, 6.44 °C/s, respectively. As for 32.1–33.4–34.5 wt% Li_2CO_3–Na_2CO_3–K_2CO_3, *TRR* increases from 2.82 °C/s to 5.02 °C/s from 450 °C to 600 °C. Considering that the maximum migration depth

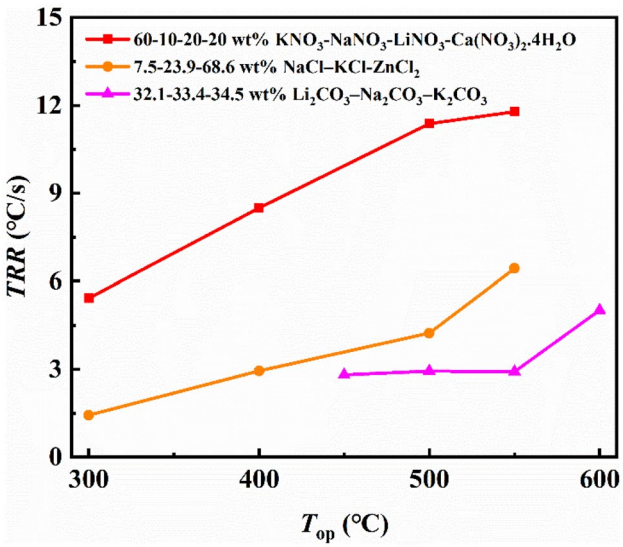

Fig. 7 Influence of operating temperature on the average temperature rising rate of the tank foundation

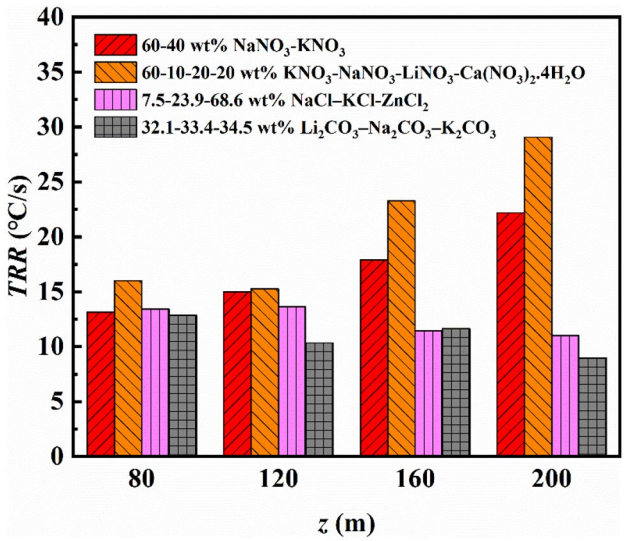

Fig. 8 Influence of molten salt type on the average temperature rising rate of the tank foundation

of 32.1–33.4–34.5 wt% Li_2CO_3–Na_2CO_3–K_2CO_3 is only 223 mm at 500 °C, in order to discuss the influence of molten salt type on *TRR* of the tank foundation, *TRR* at $z = 80$ mm, $z = 120$ mm, $z = 160$ mm and $z = 200$ mm within 10 s after contacting the molten salt is shown in Fig. 8. There is significant difference in *TRR* when different molten salts leak. The reason is that the melting point and thermal conductivity of each molten salt are different. The lower the melting point and the better the thermal conductivity, the higher *TRR* at the same position when the molten salt leaks.

3.2 Migration and phase change characteristics

3.2.1 Migration depth and width

As shown in Fig. 9, four parameters are defined to characterize the migration characteristics after the molten salt leakage. They are the distance between the top of the SMSB and the top of the fillers L_1, the length of the SMSB L_2, the maximum migration depth L_3 and the maximum migration width W_m, respectively. The influences of operating temperature on the above four parameters are presented in Fig. 10. As the operating temperature increases, the temperature of the fillers increases, leading to a further distance that the molten salt can migrate to. Therefore, the maximum migration depths of the three molten salts increase with the increase of operating temperature. For 60–10-20–20 wt% KNO_3-$NaNO_3$-$LiNO_3$-$Ca(NO_3)_2.4H_2O$ and 7.5–23.9–68.6 wt% NaCl–KCl-$ZnCl_2$, from 300 °C to 550 °C, the maximum migration depths increase from 560 mm, 247 mm to 700 mm, 405 mm respectively, and the growth rates are 25.0% and 64.0% respectively. It

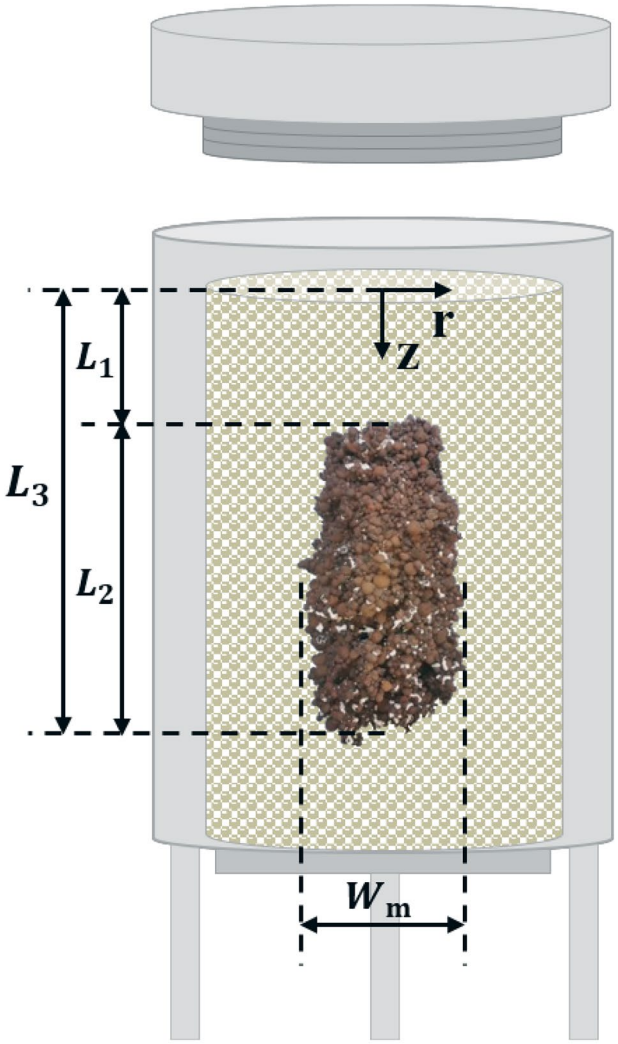

Fig. 9 Schematic diagram of the solid molten salt block formed in the tank foundation after the molten salt leakage

is worth mentioning that the bottom of the SMSB of 60–10-20–20 wt% KNO_3-$NaNO_3$-$LiNO_3$-$Ca(NO_3)_2.4H_2O$ has reached the bottom of the tank. In fact, due to the low melting point, the bottom of the SMSB of 60–10-20–20 wt% KNO_3-$NaNO_3$-$LiNO_3$-$Ca(NO_3)_2.4H_2O$ has reached the bottom of the tank at 500 °C. Thus, the maximum migration depth of 60–10-20–20 wt% KNO_3-$NaNO_3$-$LiNO_3$-$Ca(NO_3)_2.4H_2O$ no longer changes with the operating temperature after 500 °C. For 32.1–33.4–34.5 wt% Li_2CO_3–Na_2CO_3–K_2CO_3, from 450 °C to 600 °C, the maximum migration depth increases from 203 to 324 mm, and the growth rate is 59.6%. The maximum migration widths of the three molten salts decrease with the increase of the operating temperature. From 300 °C to 550 °C, the maximum migration widths of 60–10-20–20 wt% KNO_3-$NaNO_3$-$LiNO_3$-$Ca(NO_3)_2.4H_2O$ and 7.5–23.9–68.6 wt% NaCl–KCl-$ZnCl_2$ are reduced from 125 mm, 139 mm

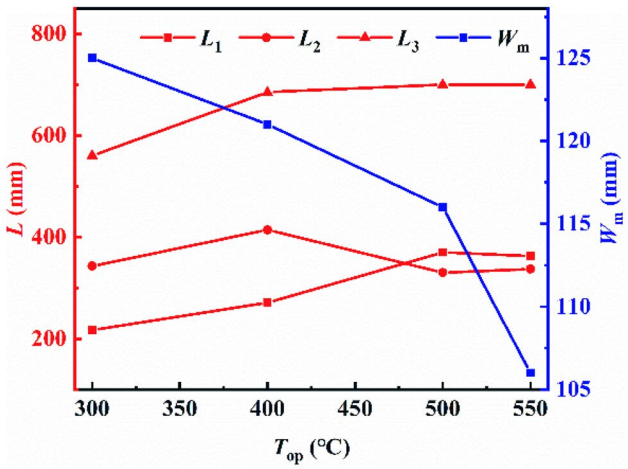

(a) 60-10-20-20 wt% KNO_3-$NaNO_3$-$LiNO_3$-$Ca(NO_3)_2.4H_2O$

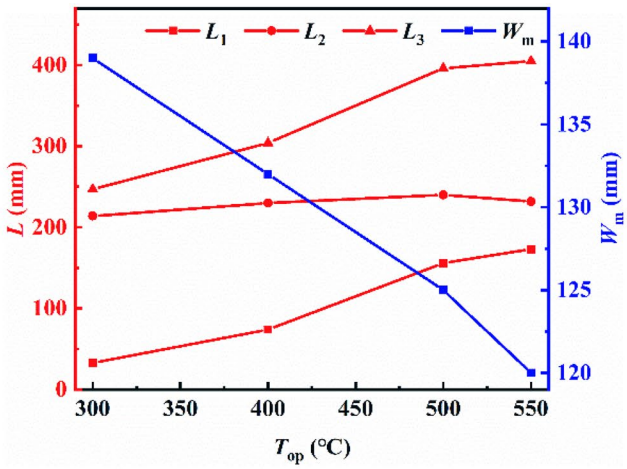

(b) 7.5-23.9-68.6 wt% NaCl–KCl-$ZnCl_2$

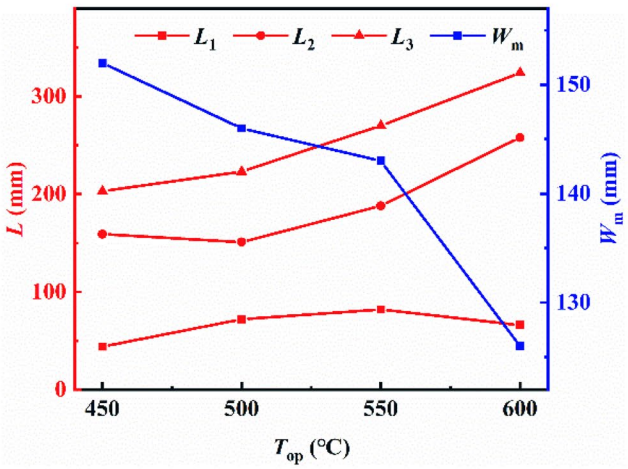

(c) 32.1-33.4-34.5 wt% Li_2CO_3–Na_2CO_3–K_2CO_3

Fig. 10 Influence of operating temperature on the migration characteristics of three potential molten salts

to 106 mm, 120 mm respectively, and the reduction rates are 15.2% and 13.7% respectively. When the operating temperature rises from 450 °C to 600 °C, the maximum migration width of 32.1–33.4–34.5 wt% Li_2CO_3–Na_2CO_3–K_2CO_3 decreases from 152 to 126 mm, and the reduction rate is 17.1%. The above results of the influence of the operating temperature on the migration characteristics of the molten salt are consistent with the results of published literatures [19, 24, 25].

Figure 11 shows the influence of the molten salt type on the migration characteristics of the molten salt at 500 °C. The maximum migration depths of Solar Salt, 60–10-20–20 wt% KNO_3-$NaNO_3$-$LiNO_3$-$Ca(NO_3)_2.4H_2O$, 7.5–23.9–68.6 wt% NaCl–KCl-$ZnCl_2$, and 32.1–33.4–34.5 wt% Li_2CO_3–Na_2CO_3–K_2CO_3 are 448 mm, 700 mm, 396 mm and 223 mm, respectively. The migration characteristics of the molten salt are mainly affected by its melting point, viscosity and heat capacity. The melting point of 60–10-20–20 wt% KNO_3-$NaNO_3$-$LiNO_3$-$Ca(NO_3)_2.4H_2O$ is significantly lower than other molten salts, so its maximum migration depth is the largest. Compared with Solar Salt, its maximum migration depth is 56.3% higher. Although the melting point of 7.5–23.9–68.6 wt% NaCl–KCl-$ZnCl_2$ is slightly lower than that of Solar Salt, its viscosity is larger than that of Solar Salt, so its maximum migration depth is 11.6% lower than that of Solar Salt. The melting point of 32.1–33.4–34.5 wt% Li_2CO_3–Na_2CO_3–K_2CO_3 is significantly higher than that of other molten salts, so its maximum migration depth is the lowest, which is 50.2% lower than that of Solar Salt. Since the mass of the molten salt leakage is constant, the migration

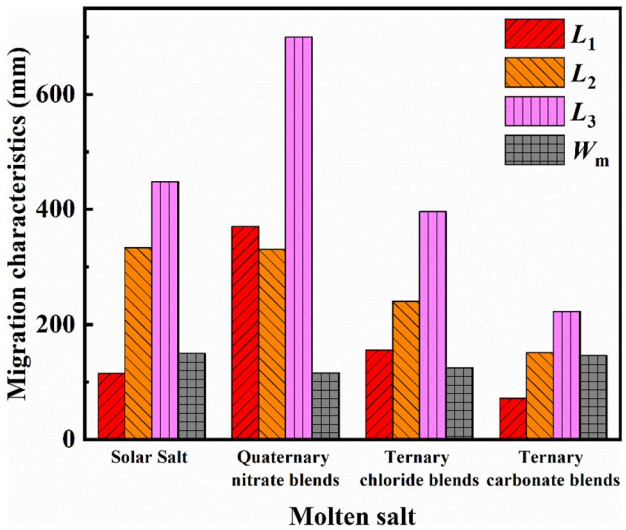

Fig. 11 Influence of molten salt type on the migration characteristics of molten salt. (T_{op} = 500 ℃)

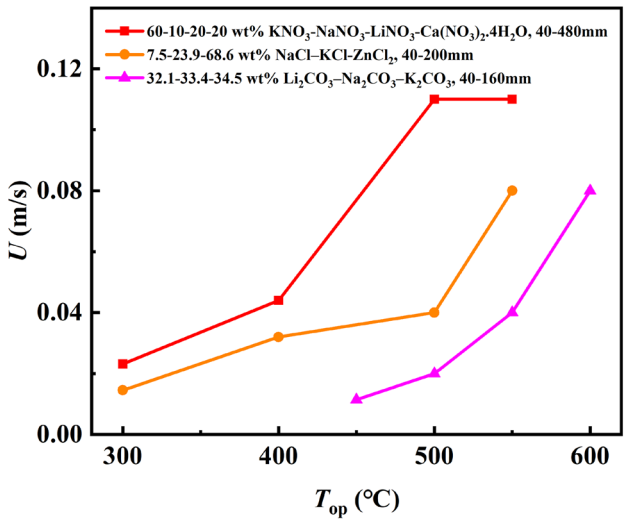

Fig. 12 Influence of operating temperature on the average migration speed of three potential molten salts

width of the molten salt with greater migration depth should generally be lower. The maximum migration widths of 60–10-20–20 wt% KNO_3-$NaNO_3$-$LiNO_3$-$Ca(NO_3)_2$.$4H_2O$, 7.5–23.9–68.6 wt% NaCl–KCl-$ZnCl_2$, and 32.1–33.4–34.5 wt% Li_2CO_3–Na_2CO_3–K_2CO_3 satisfy this rule, which is 116 mm, 125 mm, and 146 mm, respectively. The maximum migration depth of Solar Salt is larger than that of 7.5–23.9–68.6 wt% NaCl–KCl-$ZnCl_2$ and 32.1–33.4–34.5 wt% Li_2CO_3–Na_2CO_3–K_2CO_3. However, considering the melting point, viscosity and heat capacity, its maximum migration width is the largest, which is 150 mm. To sum up, compared with Solar Salt, the maximum migration widths of 60–10-20–20 wt% KNO_3-$NaNO_3$-$LiNO_3$-$Ca(NO_3)_2$.$4H_2O$, 7.5–23.9–68.6 wt% NaCl–KCl-$ZnCl_2$, and 32.1–33.4–34.5 wt% Li_2CO_3–Na_2CO_3–K_2CO_3 are reduced by 22.7%, 16.7%, and 2.7%, respectively.

3.2.2 Migration speed

The influence of the operating temperature on the average migration speed of the three potential molten salts in the tank foundation is shown in Fig. 12. For all three molten salts, the average migration speeds increase with the increase of the operating temperature. As the operating temperature increases, the time that the molten salt solidifies in the tank foundation and hinders the downward flow of the upper molten salt is relatively late, so the migration speed is relatively large. As mentioned in the previous section, the average migration speed of 60–10-20–20 wt% KNO_3-$NaNO_3$-$LiNO_3$-$Ca(NO_3)_2$.$4H_2O$ no longer increases from 500 °C to 550 °C. From 300 °C to 500 °C, the average migration speed of 60–10-20–20 wt% KNO_3-$NaNO_3$-$LiNO_3$-$Ca(NO_3)_2$.$4H_2O$ increases from 0.023 m/s to 0.11 m/s. From 300 °C to 550 °C, the average migration speed of 7.5–23.9–68.6 wt% NaCl–KCl-$ZnCl_2$ increases from 0.015 m/s to 0.08 m/s. From 450 °C to 600 °C, the average migration speed of 32.1–33.4–34.5 wt% Li_2CO_3–Na_2CO_3–K_2CO_3 increases from 0.011 m/s to 0.08 m/s when the operating temperature increases.

3.2.3 Solid molten salt block

In order to understand the change in the shape of the SMSB, a model explaining the solidification and agglomeration of the molten salt in the tank foundation is proposed in this section. As shown in Fig. 13, during the migration and phase change of the molten salt, the tank foundation can be divided into four zones from top to bottom, including the non-solidification zone, main solidification zone, secondary solidification zone and no molten salt zone. At the solidification starting position of the main solidification zone, the temperature of the filler is near the melting point of the molten salt, but the molten salt will not completely solidify temporarily for the high temperature here and will continue to migrate downward. When migrating to the solidification concentration position, the molten salt solidifies, accumulates and agglomerates here. After that, the downward flow of the upper molten salt is hindered. As a result, from this position upwards, the molten salt gradually solidifies and agglomerates in the main solidification zone. However, there is still a small part of the molten salt that can pass through the solidification concentration position to enter the secondary solidification zone, and this part of the molten salt all solidifies and agglomerates in this zone. Because the mass

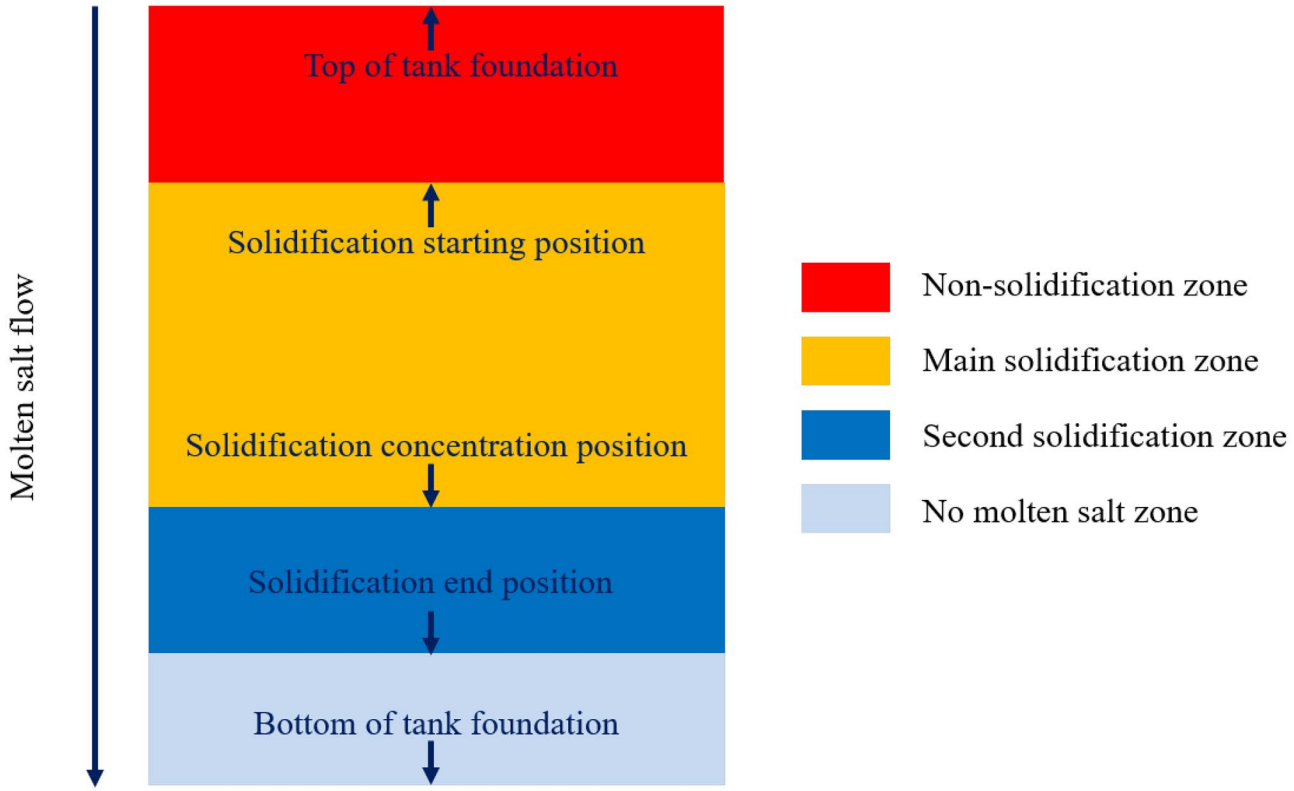

Fig. 13 Solidification and agglomeration model of molten salt leaking into the tank foundation material

of the molten salt in the main solidification zone is far more than that in the secondary solidification zone, the width of the SMSB in the main solidification zone is larger than that in the secondary solidification zone. The mass distribution of molten salt in the main solidification zone and secondary solidification zone is closely related to its melting point, viscosity and heat capacity.

The solid molten salt block formed by the molten salt and LECA after the cooling process under various experimental conditions is shown in Fig. 14. Due to the low melting point, the shape of the SMSB formed by 60–10-20–20 wt% KNO_3-$NaNO_3$-$LiNO_3$-$Ca(NO_3)_2.4H_2O$ show a transition from the thick upper part and thin lower part to the thin upper part and thick lower part as the operating temperature increases. The reason for the phenomenon is that the molten salt solidifies at the solidification concentration position and the downward flow of the upper molten salt is hindered. However, a small part of the molten salt can still pass through the position and enter the secondary solidification zone. So the shape of the SMSB is thick in the upper part and thin in the lower part. When the operating temperature increases, the maximum migration depth increases. Thus, the main solidification zone becomes longer and more molten salts distribute in the secondary solidification zone. So the upper part and lower part of the SMSB become thinner and thicker, respectively. For 7.5–23.9–68.6 wt% NaCl–KCl-$ZnCl_2$, due to its high melting point, the molten salt all solidifies in the main solidification zone at the low operating temperature. Therefore, the SMSB has a thin upper part and a thick lower part. As the operating temperature increases, a small part of the molten salt is able to enter the secondary solidification zone, so the width of the bottom of the SMSB becomes thinner. Since the melting point of Solar Salt is slightly higher than that of 7.5–23.9–68.6 wt% NaCl–KCl-$ZnCl_2$, the shape of the SMSB of Solar Salt is similar to that of case C2. Because the melting point is too high, 32.1–33.4–34.5 wt% Li_2CO_3–Na_2CO_3–K_2CO_3 solidifies quickly in the tank foundation and cannot enter the secondary solidification zone for all cases. As the operating temperature increases, the main solidification zone becomes longer. So the thickness of the upper part and lower part is almost the same when the operating temperature is below 600 ℃, while the upper part is thinner than the lower part when the operating temperature reaches 600 ℃. The experimental results well prove the validity of the above solidification and agglomeration model of the molten salt.

Fig. 14 Solid molten salt block formed by molten salt and LECA under various experimental conditions

4 Conclusions

In this paper, the leakage characteristics of three potential molten salts in the thermal tank foundation material have been experimentally studied and compared with the Solar Salt. The following conclusions are obtained.

(1) During the migration and phase change of the molten salt, due to the rapid migration of the molten salt in the tank foundation material, the temperature at each position where the molten salt flowing through first rises rapidly to the maximum value, and then decreases rapidly for the molten salt continues to migrate downward and dissipates heat. The steady temperature of the tank foundation after the leakage of molten salt is higher than that before the leakage.

(2) In the area of the molten salt flowing through, the temperature rising rate from top to bottom increases first and then decreases, and the position with the highest temperature rising rate gradually shifts downward as the operating temperature increases.

(3) The operating temperature and molten salt type significantly affect both the temperature rising rate of tank foundation and migration and phase change characteristics of the molten salt. Increasing the operating temperature, the average temperature rising rate, maximum migration depth, maximum migration width and migration speed respectively increase, increase, decrease and increase. The molten with lower melting point and better thermal conductivity leads to a higher temperature rising rate during its migration. Compared with Solar Salt, the maximum migration depths of 60–10-20–20 wt% KNO_3-$NaNO_3$-$LiNO_3$-$Ca(NO_3)_2.4H_2O$, 7.5–23.9–68.6 wt% NaCl–KCl-$ZnCl_2$, and 32.1–33.4–34.5 wt% Li_2CO_3–Na_2CO_3–K_2CO_3 increase 56.3%, -11.6%, and -50.2%, and the maximum migration widths increase -22.7%, -16.7%, and -2.7%, respectively.

(4) A model of the solidification and agglomeration of the molten salt in tank foundation is proposed, and the experimental results of the shape change of the solid molten salt blocks of the three molten salts well prove its validity. The shape of SMSB is closely related to the melting point, viscosity and heat capacity of the molten salt.

Acknowledgements The Project is supported by the National Natural Science Foundation of China (52036008).

Authors contribution Yuhang Zuo: Conceptualization, Methodology, Investigation, Data curation, Writing—original draft, Writing—review & editing, Visualization. Hao Zhou: Conceptualization, Methodology, Resources, Supervision, Project administration, Funding acquisition. Mingrui Zhang: Investigation. Fangzheng Cheng: Investigation. Hua Shi: Investigation.

Data availability The data that support the findings of this study are available from the corresponding author upon reasonable request.

Declaration

Competing interest The authors declare that they have no known competing financial interests or personal relationships that could have appeared to influence the work reported in this paper.

References

1. Pelay U, Luo L, Fan Y et al (2017) Thermal energy storage systems for concentrated solar power plants. Renew Sustain Energy Rev 79:82–100. https://doi.org/10.1016/j.rser.2017.03.139
2. Bonk A, Sau S, Uranga N et al (2018) Advanced heat transfer fluids for direct molten salt line-focusing CSP plants. Prog Energy Combust Sci 67:69–87. https://doi.org/10.1016/j.pecs.2018.02.002
3. Zhou H, Zuo Y, Zhou M, Li Y (2021) Coupled optical and thermal simulation of the thermal performance of a 50 MWe external cylindrical solar receiver. J Renew Sustain Energy 13:023704. https://doi.org/10.1063/5.0043763
4. González-Roubaud E, Pérez-Osorio D, Prieto C (2017) Review of commercial thermal energy storage in concentrated solar power plants: Steam vs. molten salts. Renew Sustain Energy Rev 80:133–148. https://doi.org/10.1016/j.rser.2017.05.084
5. Achkari O, El Fadar A (2020) Latest developments on TES and CSP technologies – Energy and environmental issues, applications and research trends. Appl Therm Eng 167:114806. https://doi.org/10.1016/j.applthermaleng.2019.114806
6. Li Y, Xu X, Wang X et al (2017) Survey and evaluation of equations for thermophysical properties of binary/ternary eutectic salts from NaCl, KCl, MgCl2, CaCl2, ZnCl2 for heat transfer and thermal storage fluids in CSP. Sol Energy 152:57–79. https://doi.org/10.1016/j.solener.2017.03.019
7. Vignarooban K, Xu X, Arvay A et al (2015) Heat transfer fluids for concentrating solar power systems - A review. Appl Energy 146:383–396. https://doi.org/10.1016/j.apenergy.2015.01.125
8. Mohan G, Venkataraman MB, Coventry J (2019) Sensible energy storage options for concentrating solar power plants operating above 600 °C. Renew Sustain Energy Rev 107:319–337. https://doi.org/10.1016/j.rser.2019.01.062
9. Prieto C, Fereres S, Ruiz-Cabañas FJ et al (2020) Carbonate molten salt solar thermal pilot facility: Plant design, commissioning and operation up to 700 °C. Renew Energy 151:528–541. https://doi.org/10.1016/j.renene.2019.11.045
10. Mehos M, Turchi C, Vidal J et al (2017) Concentrating solar power Gen3 demonstration roadmap (No. NREL/TP-5500-67464). National Renewable Energy Lab (NREL). Golden, CO, United States. https://doi.org/10.2172/1338899
11. Fernández AG, Pineda F, Walczak M, Cabeza LF (2019) Corrosion evaluation of alumina-forming alloys in carbonate molten salt for CSP plants. Renew Energy 140:227–233. https://doi.org/10.1016/j.renene.2019.03.087
12. Fernández AG, Gomez-Vidal J, Oró E et al (2019) Mainstreaming commercial CSP systems: A technology review. Renew Energy 140:152–176. https://doi.org/10.1016/j.renene.2019.03.049
13. Olivares RI, Chen C, Wright S (2012) The thermal stability of molten lithium–sodium–potassium carbonate and the influence of additives on the melting point. J Sol Energy Eng Trans ASME 134(4). https://doi.org/10.1115/1.4006895
14. Li P, Molina E, Wang K et al (2016) Thermal and Transport Properties of NaCl-KCl-ZnCl2 Eutectic Salts for New Generation High-Temperature Heat-Transfer Fluids. J Sol Energy Eng Trans ASME 138:1–8. https://doi.org/10.1115/1.4033793
15. Vignarooban K, Pugazhendhi P, Tucker C et al (2014) Corrosion resistance of Hastelloys in molten metal-chloride heat-transfer fluids for concentrating solar power applications. Sol Energy 103:62–69. https://doi.org/10.1016/j.solener.2014.02.002
16. Vignarooban K, Xu X, Wang K et al (2015) Vapor pressure and corrosivity of ternary metal-chloride molten-salt based heat transfer fluids for use in concentrating solar power systems. Appl Energy 159:206–213. https://doi.org/10.1016/j.apenergy.2015.08.131
17. Ren N, Wu YT, Ma CF, Sang LX (2014) Preparation and thermal properties of quaternary mixed nitrate with low melting point. Sol Energy Mater Sol Cells 127:6–13. https://doi.org/10.1016/j.solmat.2014.03.056
18. Wei X, Qin B, Yang C et al (2019) Nox emission of ternary nitrate molten salts in high-temperature heat storage and transfer process. Appl Energy 236:147–154. https://doi.org/10.1016/j.apenergy.2018.11.087
19. Zhou H, Shi H, Lai Z et al (2020) Migration and phase change study of leaking molten salt in tank foundation material. Appl Therm Eng 170. https://doi.org/10.1016/j.applthermaleng.2020.114968
20. Dawson M, Borman D, Hammond RB et al (2014) Moving boundary models for the growth of crystalline deposits from undetected leakages of industrial process liquors. Comput Chem Eng 71:331–346. https://doi.org/10.1016/j.compchemeng.2014.08.011
21. Song M, Viskanta R (2001) Lateral freezing of an anissotropic porous medium saturated with an aqueous salt solution. Int J Heat Mass Transf 44:733–751. https://doi.org/10.1016/S0017-9310(00)00132-0
22. Weisbrod N, Niemet MR, Rockhold ML et al (2004) Migration of saline solutions in variably saturated porous media. J Contam Hydrol 72:109–133. https://doi.org/10.1016/j.jconhyd.2003.10.013
23. Shan J, Ding J, Lu J (2015) Numerical Investigation of High-temperature Molten Salt Leakage. Energy Procedia 69:2072–2080. https://doi.org/10.1016/j.egypro.2015.03.221
24. Wu J, Ding J, Lu J, Wang W (2017) Migration and phase change phenomena and characteristics of molten salt leaked into soil porous system. Int J Heat Mass Transf 111:312–320. https://doi.org/10.1016/j.ijheatmasstransfer.2017.04.002
25. Zhang Y, Wu J, Wang W et al (2019) Experimental and numerical studies on molten salt migration in porous system with phase change. Int J Heat Mass Transf 129:397–405. https://doi.org/10.1016/j.ijheatmasstransfer.2018.09.122

26. An X, Cheng J, Zhang P et al (2016) Determination and evaluation of the thermophysical properties of an alkali carbonate eutectic molten salt. Faraday Discuss 190:327–338. https://doi.org/10.1039/c5fd00236b
27. Bonilla J, Rodríguez-García MM, Roca L et al (2018) Design and experimental validation of a computational effective dynamic thermal energy storage tank model. Energy 152:840–857. https://doi.org/10.1016/j.energy.2017.11.017
28. Zhou H, Shi H, Zhang J, Zhou M (2020) Experimental and numerical investigation of temperature distribution and heat loss of molten salt tank foundation at different scales. Heat Mass Transf und Stoffuebertragung 56:2859–2869. https://doi.org/10.1007/s00231-020-02905-x